Spin Current Generation by Spin Pumping 36

Kazuya Ando and Eiji Saitoh

Contents

Abstract

Magnetization dynamics is coupled with spin currents by exchanging the spin-angular momentum. This coupling allows to control magnetization by spin currents; spin injection into a ferromagnet induces magnetization precession. The inverse of this process, namely, spin current emission from precessing magnetization, is spin pumping, which offers a route for generating spin currents in a wide range of materials. This chapter describes experiments on the generation and detection of spin currents using the spin pumping and inverse spin-Hall effect. The inverse spin-Hall effect, conversion of spin currents into an electric voltage through spin-orbit interaction, induced by the spin pumping was first discovered in a metallic film. The spin pumping in this film is quantitatively

K. Ando (✉)
Department of Applied Physics and Physico-Informatics, Keio University, Yokohama, Japan
e-mail: ando@appi.keio.ac.jp

E. Saitoh
Institute for Materials Research, Tohoku University, Sendai, Japan
e-mail: eizi@imr.tohoku.ac.jp

Y. Xu et al. (eds.), *Handbook of Spintronics*,
DOI 10.1007/978-94-007-6892-5_52

consistent with a model calculation based on the Landau-Lifshitz-Gilbert equation. This dynamical spin injection, the spin pumping, offers an easy and versatile way for injecting spin currents into not only metals but also high-resistivity materials. In a metal/semiconductor junction, the spin pumping is demonstrated to be controlled electrically through the tuning of dynamical spin-exchange coupling at the interface. This spin-injection method works without applying a charge current, which makes it possible to generate spin currents from magnetic insulators; the spin pumping appears even in a metal/insulator junction due to finite spin-exchange interaction at the interface. The spin pumping from an insulator enables nonlinear generation of spin currents: nonlinear spin pumping. The combination of the spin pumping and inverse spin-Hall effect provides an essential route for exploring spin physics in condensed matter.

List of Abbreviations

FMR	Ferromagnetic resonance
ISHE	Inverse spin-Hall effect
LLG	Landau-Lifshitz-Gilbert

Introduction

A spin current interacts with magnetization by exchanging the spin-angular momentum [1]. This interaction enables to control magnetization using a spin current; spin injection into a ferromagnet transfers the spin-angular momentum of the spin current to the magnetization, driving magnetization precession without external rf magnetic fields. The inverse of this process is the spin pumping [2, 3]; when magnetization precession is maintained by an external rf magnetic field, a spin current is emitted from the precessing magnetization in a ferromagnetic/nonmagnetic (F/N) junction through dynamical spin-exchange interaction between the magnetization in the F layer and the carrier spins in the N layer.

In a F/N junction, magnetization in the F layer and electron spins in the N layer interact at the interface through the s-d interaction: $H_{\mathrm{sd}} = -J_{\mathrm{sd}}\sum_{i\in I}\mathbf{S}_i\mathbf{s}_i$, where $\mathbf{S}_i$ and $\mathbf{s}_i$ are the localized spin of the F layer and the conduction electron spin in the N layer at site i on the interface. J_{sd} is the exchange coupling strength between $\mathbf{S}_i$ and $\mathbf{s}_i$. Assuming that the magnetic moments in the F layer are strongly coupled with each other so that all magnetic moments coherently precess around the z direction, one can replace $\mathbf{S}_i$ by the magnetization $\mathbf{M}$ with the relation $\mathbf{S}_i/S = \mathbf{M}/M_s$. Thus, the s-d interaction is expressed as $H_{\mathrm{sd}} = -J_{\mathrm{ex}}\int dx\mathbf{M}_I\bullet\mathbf{m}_N(x)$, where x axis is directed normal to the interface. Here, $J_{\mathrm{ex}} = J_{\mathrm{sd}}S/(\hbar\gamma_e M_s)$ is the dimensionless exchange coupling constant, M_s is the saturation magnetization, S is an effective block spin per unit cell, and γ_e is the gyromagnetic ratio of conduction electrons. $\mathbf{m}_N = \hbar\gamma_e\mathbf{s}_N$ is the induced magnetization of the N layer. $\mathbf{s}_N = \mathbf{s}_i/v_e$ is the spin density in the N layer, where v_e is the volume per electrons in the N layer. $\mathbf{M}_I = \mathbf{M}_\delta(t)\delta(x - x_0) = \mathbf{M}(t)a_{\mathrm{eff}}\delta(x - x_0)$ is the interface magnetization, where $\mathbf{M}(x,t) = \mu_a(t)\sum_l \delta(\mathbf{r}-\mathbf{r}_l) = \mathbf{M}_\delta(t)\sum_i (x-x_i) = \mathbf{M}(t)a_S\sum_i \delta(x-x_i)$ with$\mathbf{M}(t) = \mathbf{M}_\delta(t)/a_S = \mu_a(t)/a_S^3$. Here, $\mathbf{M}_\delta$ is the sheet magnetization and μ_a is the magnetic moment at cite. $\mathbf{r}_l.a_{\text{eff}} = v_e/a_s^2$ is the effective interaction range. The exchange coupling exerts a torque on $\mathbf{m}_N(x,t)$. Thus, one may write the dynamics of the magnetization and the electron spin as [4]

$$\frac{\partial \mathbf{M}}{\partial t} = -\gamma(\mathbf{M}\times\mathbf{H}_{\text{eff}}) - \gamma(\mathbf{M}_I \times J_{\text{ex}}\mathbf{m}_N) + \frac{\alpha}{M_s}\mathbf{M}\times\frac{\partial \mathbf{M}}{\partial t}, \tag{1}$$

$$\frac{\partial \mathbf{m}_{\text{N}}}{\partial t} = -\gamma_e(\mathbf{m}_N \times J_{\text{ex}}\mathbf{M}_I) - \frac{\delta \mathbf{m}_N}{\tau_N^{\text{sf}}} + D_N\nabla^2\delta\mathbf{m}_N, \tag{2}$$

where γ and α are the gyromagnetic ratio and the Gilbert damping constant, respectively. τ_N^{sf} and D_N are the spin relaxation time and diffusion constant in the N layer, respectively. Here, the magnetization of conduction electrons in the N layer $\mathbf{m}_N(x,t)$ is written as $\mathbf{m}_N(x,t) = \chi_N J_{\text{ex}}\mathbf{M}(x,t) + \delta\mathbf{m}_N(x,t)$ with the nonequilibrium magnetization, or spin accumulation, $\delta\mathbf{m}_\mathbf{N}$ in the N layer. χ_N is the Pauli susceptibility. The second term in Eq. 1 and the first term in Eq. 2 represent the exchange torque at the interface. The spin relaxation and spin diffusion in the N layer are described in the third and forth terms in Eq. 2. A solution of Eq. 2 has the form

$$\delta\mathbf{m}(x) = -\frac{\chi_N}{\gamma_e}\frac{1}{1+\Gamma^2}\left(\Gamma\frac{d}{dt}\hat{\mathbf{M}} + \hat{\mathbf{M}}\times\frac{d}{dt}\hat{\mathbf{M}}\right)e^{-x/\lambda_N}, \tag{3}$$

where $\hat{\mathbf{M}} = \mathbf{M}/M_s$ and $\Gamma = \hbar\lambda_N/\left(SJ_{sd}\tau_N^{\text{sf}}a_{\text{eff}}\right).\lambda_N = \sqrt{D_N\tau_N^{\text{sf}}}$ is the spin-diffusion length. The z component of the spin accumulation is given by $\delta m_z(x) = -(1/g_e)$ $(\mu_B N_N(0)\hbar)/\left(1+\Gamma^2\right)\left[\hat{\mathbf{M}}\times(d/dt)\hat{\mathbf{M}}\right]_z$, where g_e is the electron g factor. $\chi_N = \mu_B^2 N_N(0)$, where $N_N(0)$ is the density of states at the Fermi energy. Therefore, a spin current with the spin-polarization direction along the z axis, $j_s = (-e/\mu_B)D_N\nabla\delta m_N^z$, is obtained as

$$j_s^z(x) = \frac{\hbar^2 D_N N_N(0)}{2g_e\lambda_N\left(1+\Gamma^2\right)}\left[\mathbf{M}(t)\times\frac{d\mathbf{M}(t)}{dt}\right]_z e^{-x/\lambda_N}, \tag{4}$$

or, using the spin-pumping conductance $g_r^{\uparrow\downarrow}$, the direct-current component of the spin current at the F/N interface ($x = 0$) can be expressed as [2]

$$j_s = \frac{\omega}{2\pi}\int_0^{2\pi/\omega}\frac{\hbar}{4\pi}g_r^{\uparrow\downarrow}\frac{1}{M_s^2}\left[\mathbf{M}(t)\times\frac{d\mathbf{M}(t)}{dt}\right]_z dt. \tag{5}$$

The spin pumping allows to explore the physics of a spin current in a wide range of materials, making it a key technique in spintronics as discussed below.

Electric Detection of Spin Pumping in Metallic Film

Spin currents generated by the spin pumping can be detected using the inverse spin-Hall effect (ISHE), which converts a spin current into an electric field through spin-orbit interaction as [5]

$$\mathbf{E}_{\mathrm{ISHE}} = (\theta_{\mathrm{SHE}}\rho_{\mathrm{N}})\mathbf{j}_{\mathrm{s}} \times \sigma. \tag{6}$$

Here, $\theta_{\mathrm{SHE}} = \sigma_{\mathrm{SHE}}/\sigma_{\mathrm{N}}$ is the spin-Hall angle, where σ_{SHE} and σ_{N} are the spin-Hall conductivity and electric conductivity, respectively. ρ_{N} is the electric resistivity. The ISHE enables electric detection of spin currents even in the absence of spin accumulation, making it a key technique for exploring spin currents. The ISHE induced by the spin pumping was first discovered in a $Ni_{81}Fe_{19}$/Pt film [5]. The following describes the details of the experimental procedure and results obtained in a $Ni_{81}Fe_{19}$/Pt film [6, 7].

The sample used for the measurements is a $Ni_{81}Fe_{19}$/Pt film comprising a 10-nm-thick ferromagnetic $Ni_{81}Fe_{19}$ layer (a 0.4 × 1.2 mm rectangular shape) and a 10-nm-thick paramagnetic Pt layer (a 0.4 × 2.2 mm rectangular shape) (see Fig. 1a). These layers were patterned using metal masks. The Pt layer was fabricated by sputtering on a thermally oxidized Si substrate, and then the $Ni_{81}Fe_{19}$ layer was evaporated on the Pt layer in a high vacuum. Two electrodes are attached to both ends of the Pt layer. For the measurement, the sample was placed near the center of a TE_{011} cavity at which the magnetic-field component of the microwave mode is maximized, while the electric-field component is minimized. During the measurement, a microwave mode with frequency $f = 9.44$ GHz existed in the cavity, and the external magnetic field **H** was applied perpendicular to the direction across the electrodes. All the measurements were performed at room temperature.

Figure 1b shows microwave absorption spectra $dI(H)/dH$ measured for the $Ni_{81}Fe_{19}$/Pt film and a $Ni_{81}Fe_{19}$ film where the Pt layer is missing. Here, I denotes the microwave absorption intensity. As shown in Fig. 1b, the spectral width W (see the inset to Fig. 1b) for the $Ni_{81}Fe_{19}$ film is clearly enhanced by attaching the Pt layer. This result shows that the magnetization-precession relaxation is enhanced by attaching the Pt layer, since the spectral width W is proportional to the Gilbert damping constant α [8]. This spectral width enhancement demonstrates the emission of a spin current from the precessing magnetization induced by the spin pumping; since a spin current carries spin-angular momentum, this spin current emission deprives the magnetization of the spin-angular momentum and thus gives rise to additional magnetization-precession relaxation or enhances α. The spectral width enhancement due to the spin pumping, $\Delta W = W_{F/N} - W_F$, is related with the spin-pumping conductance $g_r^{\uparrow\downarrow}$ as [9, 10]

$$\Delta W = \frac{g\mu_B\omega}{2\sqrt{3}\pi M_S\gamma d_F} g_r^{\uparrow\downarrow}, \tag{7}$$

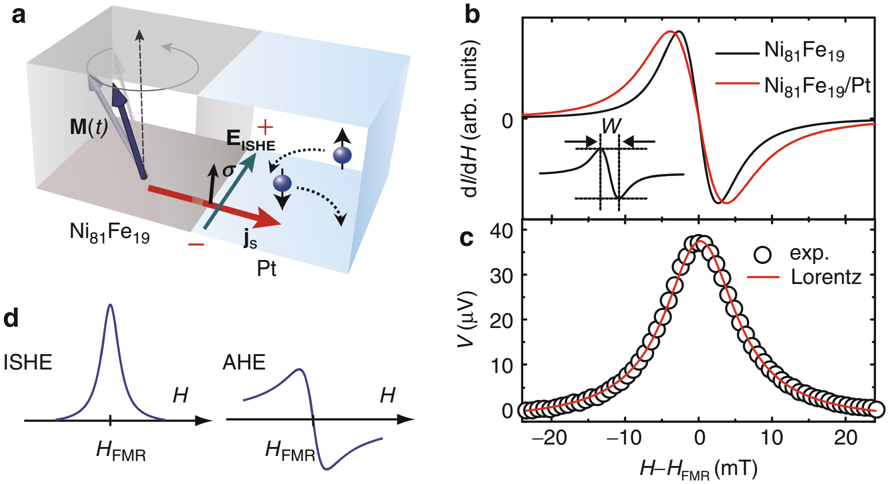

Fig. 1 (**a**) A schematic illustration of the spin pumping and the inverse spin-Hall effect in the $Ni_{81}Fe_{19}$/Pt film. **M**(t) is the magnetization in the $Ni_{81}Fe_{19}$ layer. $\mathbf{E}_{ISHE}$, $\mathbf{J}_s$, and σ denote the electromotive force due to the inverse spin-Hall effect, the spatial direction of a spin current, and the spin-polarization vector of the spin current, respectively. (**b**) Field (H) dependence of the FMR signals $dI(H)/dH$ for the $Ni_{81}Fe_{19}$/Pt film and the $Ni_{81}Fe_{19}$ film. Here, I denotes the microwave absorption intensity. H_{FMR} is the resonance field. The *inset* shows the definition of the spectral width W in the present study. (**c**) Field dependence of the electric-potential difference V for the $Ni_{81}Fe_{19}$/Pt film under the 200 mW microwave excitation. The *open circles* are the experimental data. The curve in *red* shows the fitting result using a Lorentz function for the V data. (**d**) The spectral shape of the electromotive force due to the inverse spin-Hall effect (ISHE) and the anomalous-Hall effect (AHE)

where $W_{F/N}$ and W_F are the FMR spectral width for the $Ni_{81}Fe_{19}$/Pt film and the $Ni_{81}Fe_{19}$ film, respectively. g and μ_B are the g factor and the Bohr magneton, respectively. Using the parameters $g = 2.12$, $4\pi M_s = 0.745$ T, $d_F = 10$ nm, $\gamma = 1.86 \times 10^{11}\ \mathrm{T^{-1}\ s^{-1}}$, $\omega = 5.93 \times 10^{10}\ \mathrm{s^{-1}}$, $W_{F/N} = 7.58$ mT, and $W_F = 5.34$ mT, the spin-pumping conductance at the $Ni_{81}Fe_{19}$/Pt interface is obtained as $g_r^{\uparrow\downarrow} = 2.31 \times 10^{19} \mathrm{m^{-2}}$.

The above experimental result shows that the ISHE induced by the spin pumping can be explored in the $Ni_{81}Fe_{19}$/Pt film. When H and f fulfill the FMR condition, a spin current with a spin polarization σ parallel to the magnetization-precession axis in the $Ni_{81}Fe_{19}$ layer is injected into the Pt layer by the spin pumping. This spin current is converted into an electric voltage using the strong ISHE in the Pt layer [11] as shown in Fig. 1a. The ISHE induced by the spin pumping can be detected by measuring the electric voltage.

Figure 1c shows the electromotive force signal V measured for the $Ni_{81}Fe_{19}$/Pt film under the 200 mW microwave excitation. In the V spectrum, an electromotive force signal appears around the resonance field H_{FMR}. This electromotive force is

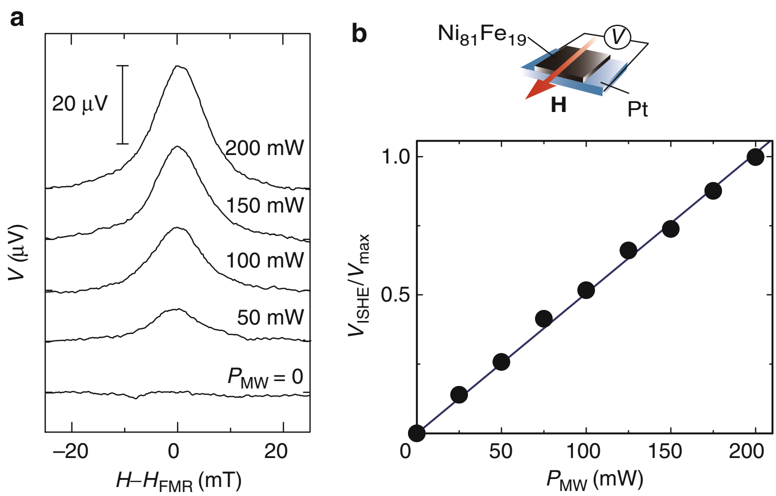

Fig. 2 (**a**) The electromotive force V spectra measured for the $Ni_{81}Fe_{19}$/Pt film at different microwave excitation powers P_{MW}. (**b**) The microwave power P_{MW} dependence of the electromotive force V_{ISHE} for the $Ni_{81}Fe_{19}$/Pt film. V_{ISHE} is estimated as the peak height of the resonance shape in the V spectrum

attributed to the ISHE induced by the spin pumping. Notably, the spectral shape of this electromotive force is well reproduced using a Lorentz function.

The symmetric shape of the electromotive force is a feature expected for the spin-pumping-induced ISHE. Although an in-plane component of a microwave electric field may induce a rectified electromotive force via the anomalous-Hall effect (AHE) in cooperation with FMR [5, 12–14], the electromotive force due to the ISHE and AHE can be distinguished in terms of their spectral shapes [15]. Since the magnitude of the electromotive force due to the ISHE induced by the spin pumping, $V_{ISHE}(H)$, is proportional to the microwave absorption intensity, $V_{ISHE}(H)$ is maximized at the FMR condition. In contrast, the sign of the electromotive force due to the AHE ($\propto \mathbf{e}(t) \times \mathbf{m}(t)$), $V_{AHE}(H)$, is reversed across the ferromagnetic resonance field H_{FMR}, where $\mathbf{e}(t)$ and $\mathbf{m}(t)$ are the microwave electric field and the magnetization component perpendicular to $\mathbf{e}(t)$, respectively, since the magnetization-precession phase shifts by π at the resonance [16]. Therefore, the electromotive force due to the ISHE and AHE is of the Lorentz shape and the dispersion shape, respectively, as shown in Fig. 1d.

The above experimental results are further buttressed by measuring microwave power and magnetic-field-angle dependence of the electromotive force. The V spectra for the $Ni_{81}Fe_{19}$/Pt film at different microwave excitation powers P_{MW} are shown in Fig. 2a. The electromotive force decreases with decreasing P_{MW}, consistent with the prediction of the spin pumping. Figure 2b shows microwave power P_{MW} dependence of the magnitude of the electromotive force V_{ISHE}, where V_{ISHE} is estimated as the peak height of the resonance shape in the V spectra. The P_{MW} dependence of V_{ISHE} shows that the amount of spin current injected into the Pt

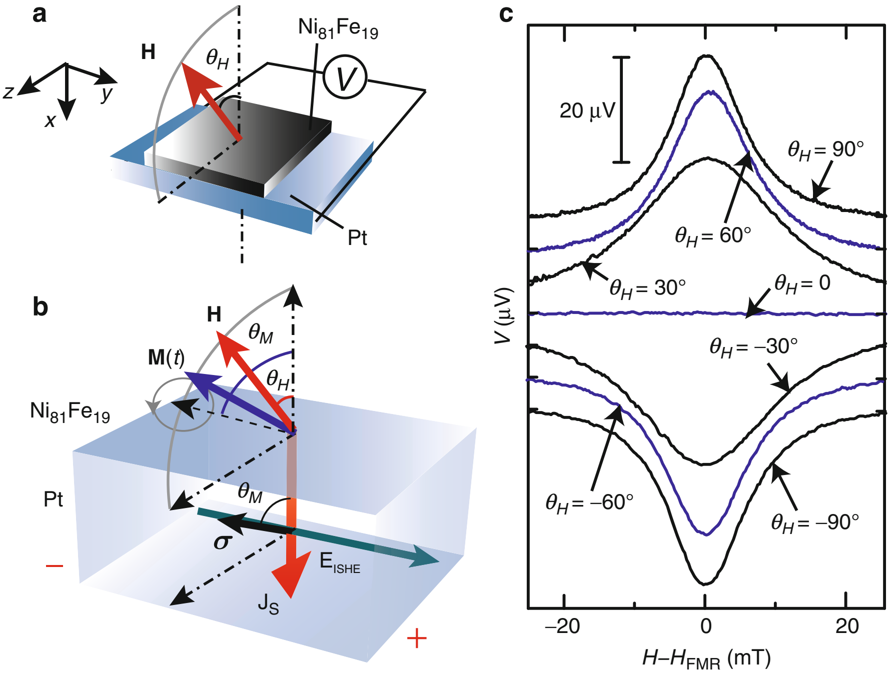

Fig. 3 (**a**) A schematic illustration of the measurement setup for the out-of-plane magnetic-field-angle dependence of the ISHE signal. θ_H is the external-magnetic-field angle to the normal vector of the film plane. (**b**) A schematic illustration of the inverse spin-Hall effect induced by the spin pumping. θ_M is the magnetization angle to the normal vector of the film plane. (**c**) The out-of-plane magnetic-field-angle θ_H dependence of the electromotive force V for the $Ni_{81}Fe_{19}$/Pt film

layer is proportional to P_{MW}. This is consistent with the prediction of a direct-current-spin-pumping model [15]. Equation 5 shows that the dc component of a spin current generated by the spin pumping is proportional to the projection of $\mathbf{M}(t) \times d\mathbf{M}(t)/dt$ onto the magnetization-precession axis. This projection is proportional to the square of the magnetization-precession amplitude. In this case, therefore, the induced spin current or the electromotive force due to the ISHE is proportional to the square of the magnetization-precession amplitude, i.e., the microwave power P_{MW}.

Figure 3c shows H dependence of V for the $Ni_{81}Fe_{19}$/Pt film at different out-of-plane magnetic-field-angle θ_H, where the external magnetic field H was applied at an angle of θ_H to the normal vector of the film plane, as shown in Fig. 3a. Notable is that, with changing θ_H, the V signal disappears at $\theta_H = 0$ and changes its sign when $\theta_H > 0$. This feature is consistent with the prediction of the spin pumping and ISHE. The spin polarization σ of a dc spin current generated by the spin pumping is directed along the magnetization-precession axis (see Fig. 3b). This spin current is converted into an electromotive force by the ISHE as $\mathbf{E}_{\mathrm{ISHE}} \propto \mathbf{J}_s \times \sigma$; the sign of the electromotive force is reversed by reversing the $\mathbf{H}$ direction. When $\theta_H = 0$, the precession axis of the magnetization in the $Ni_{81}Fe_{19}$ layer is directed along the normal axis of the film plane. In this situation, the spin-polarization vector of a spin current σ is parallel to the flow direction of the spin current $\mathbf{J}_s$, and thus Eq. 6 predicts $\mathbf{E}_{\mathrm{ISHE}} \propto \mathbf{J}_s \times \sigma = \mathbf{0}$, being consistent with the experimental result.

To quantitatively understand the out-of-plane magnetic-field-angle θ_H dependence of the V signal, in the following section, the spin current emission in thin film systems is formulated based on the Landau-Lifshitz-Gilbert (LLG) equation combined with the model of the spin pumping.

Model of Spin Pumping

The dynamics of magnetization $\mathbf{M}(t)$ in a ferromagnetic film under an effective magnetic field $\mathbf{H}_{\mathrm{eff}}$ is described by the LLG equation

$$\frac{d\mathbf{M}(t)}{dt} = -\gamma\mathbf{M}(t) \times \mathbf{H}_{\mathrm{eff}} + \frac{\alpha}{M_s}\mathbf{M}(t) \times \frac{d\mathbf{M}(t)}{dt}. \tag{8}$$

Firstly, Eq. 8 is considered in an equilibrium condition, where the equilibrium magnetization direction $\mathbf{M}$ is directed to the z axis (see Fig. 4a). Here, a soft

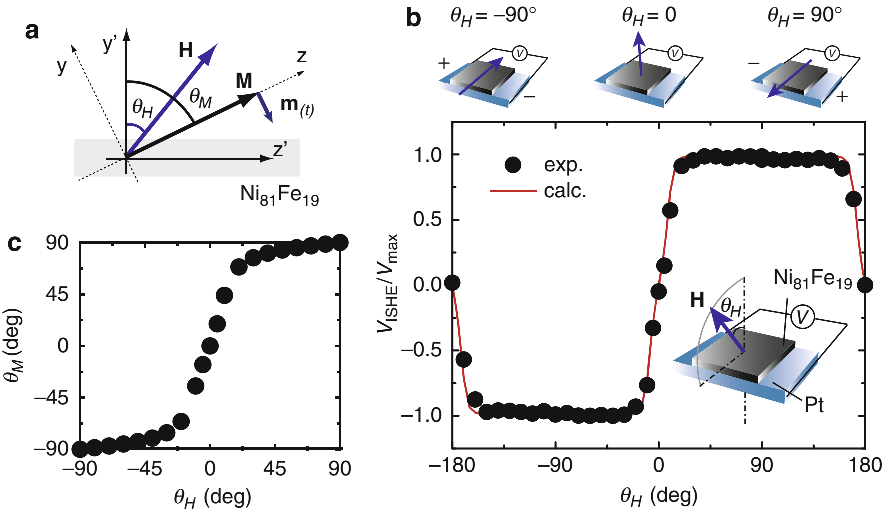

Fig. 4 (**a**) A schematic illustration of the coordinate system used for describing a ferromagnetic film. $\mathbf{M}$ and $\mathbf{m}(t)$ are the static and the dynamic components of the magnetization $\mathbf{M}(t)$. $\mathbf{H}$ is the external magnetic field. θ_H and θ_M are the external-magnetic-field angle and the magnetization angle to the normal vector of the film plane, respectively. (**b**) The out-of-plane magnetic-field-angle θ_H dependence of the ISHE signal V_{ISHE} measured for the $Ni_{81}Fe_{19}$/Pt film. $V_{\mathrm{ISHE}}/V_{\mathrm{max}}$ is the normalized spectral intensity extracted by a fitting procedure using Lorentz functions from the measured electromotive-force spectra. The *filled circles* are the experimental data. The solid curve is the theoretical curve calculated from Eq. 18. (**c**) The θ_H dependence of θ_M

ferromagnetic thin film, e.g., $Ni_{81}Fe_{19}$, is assumed, and the magnetocrystalline anisotropy is neglected. The external magnetic field $\mathbf{H}$ and the static demagnetizing field $\mathbf{H_M}$ induced by $\mathbf{M}$ are taken into account as the effective magnetic field $\mathbf{H}_{\text{eff}}$:

$$\mathbf{H}_{\text{eff}} = \mathbf{H} + \mathbf{H_M}, \tag{9}$$

where

$$\begin{aligned} \mathbf{H} &= H\begin{pmatrix} 0 \\ \sin(\theta_M - \theta_H) \\ \cos(\theta_M - \theta_H) \end{pmatrix}, \\ \mathbf{H_M} &= -4\pi M_s \cos\theta_M \begin{pmatrix} 0 \\ \sin\theta_M \\ \cos\theta_M \end{pmatrix}. \end{aligned} \tag{10}$$

θ_H and θ_M are the external-magnetic-field angle and the magnetization angle to the normal axis of the film plane, respectively (see Fig. 4a). The static equilibrium condition, namely $\mathbf{M} \times \mathbf{H}_{\text{eff}} = \mathbf{0}$, yields an expression, which relates θ_H and θ_M, as

$$2H\sin(\theta_H - \theta_M) + 4\pi M_s \sin 2\theta_M = 0, \tag{11}$$

where H is the strength of the external magnetic field.

Based on the LLG equation, the magnetization $\mathbf{M}(t)$ precession around the z axis can be formulated, where $\mathbf{M}(t) = \mathbf{M} + \mathbf{m}(t)$ as shown in Fig. 4a. $\mathbf{M}$ and $\mathbf{m}(t)$ are the static and the dynamic components of the magnetization, respectively. The external magnetic field $\mathbf{H}$, the static demagnetizing field $\mathbf{H_M}$ induced by $\mathbf{M}$, the dynamic demagnetization field $\mathbf{H_m}(t)$ induced by $\mathbf{m}(t)$, and the external ac field $\mathbf{h}(t)$ are taken into account as the effective magnetic field $\mathbf{H}_{\text{eff}}$:

$$\mathbf{H}_{\text{eff}}(t) = \mathbf{H} + \mathbf{H_M} + \mathbf{H_m}(t) + \mathbf{h}(t), \tag{12}$$

where

$$\begin{aligned} \mathbf{H_m}(t) &= -4\pi m_y(t) \sin\theta_M \begin{pmatrix} 0 \\ \sin\theta_M \\ \cos\theta_M \end{pmatrix}, \\ \mathbf{h}(t) &= \begin{pmatrix} he^{i\omega t} \\ 0 \\ 0 \end{pmatrix}. \end{aligned} \tag{13}$$

A small precession of the magnetization $\mathbf{m}(t) = (m_x e^{i\omega t}, m_y e^{i\omega t}, 0)$ around the equilibrium direction $\mathbf{M}$ is assumed as a solution of Eqs. 8 and 12. Here, $\omega = 2\pi f$, where f is the microwave frequency. The resonance condition is readily obtained by neglecting the external ac field and the damping term and by finding the eigenvalue of ω of Eq. 8. By ignoring the second-order contribution of the precession amplitude, m_x and m_y, we find the ferromagnetic resonance condition:

$$\left(\frac{\omega}{\gamma}\right)^2 = \left[H_{\mathrm{FMR}} \cos\left(\theta_H - \theta_M\right) - 4\pi M_s \cos 2\theta_M\right] \times \left[H_{\mathrm{FMR}} \cos\left(\theta_H - \theta_M\right) - 4\pi M_s \cos^2\theta_M\right]. \tag{14}$$

Here, Eq. 11 was used. The dynamic components of the magnetization $\mathbf{m}(t)$ in the FMR condition are obtained from Eqs. 8 and 12 using Eqs. 11 and 14:

$$m_x(t) = \frac{4\pi M_s h\gamma \left[2\alpha\omega \cos\omega t + \left(4\pi M_s \gamma \sin^2\theta_M + \sqrt{(4\pi M_s)^2\gamma^2 \sin^4\theta_M + 4\omega^2}\right) \sin\omega t\right]}{8\pi\alpha\omega\sqrt{(4\pi M_s)^2\gamma^2 \sin^4\theta_M + 4\omega^2}}, \tag{15}$$

$$m_y(t) = -\frac{4\pi M_s h\gamma \cos\omega t}{4\pi\alpha\sqrt{(4\pi M_s)^2\gamma^2 \sin^4\theta_M + 4\omega^2}}. \tag{16}$$

Using Eqs. 5, 15, and 16, the spin current density j_s generated by the spin pumping is obtained as

$$j_s = \frac{g_r^{\uparrow\downarrow}\gamma^2 h^2 \hbar \left(4\pi M_s \gamma \sin^2\theta_M + \sqrt{(4\pi M_s)^2\gamma^2 \sin^4\theta_M + 4\omega^2}\right)}{8\pi\alpha^2 \left((4\pi M_s)^2\gamma^2 \sin^4\theta_M + 4\omega^2\right)}. \tag{17}$$

Here, the spin-polarization vector σ of the spin current is directed along the magnetization-precession axis, since the dc component of $\mathbf{M}(t) \times d\mathbf{M}(t)/dt$ is directed along the z axis. The electromotive force due to the ISHE, V_{ISHE}, is obtained by combining Eqs. 6 and 17; V_{ISHE} is proportional to $j_s \sin\theta_M$ because of Eq. 6, since the spin-polarization vector σ of a spin current is directed along the z axis. Therefore, the ISHE signal V_{ISHE} is expressed as

$$V_{\mathrm{ISHE}} \propto \frac{g_r^{\uparrow\downarrow}\gamma^2 h^2 \hbar \sin\theta_M \left(4\pi M_s \gamma \sin^2\theta_M + \sqrt{(4\pi M_s)^2\gamma^2 \sin^4\theta_M + 4\omega^2}\right)}{8\pi\alpha^2 \left((4\pi M_s)^2\gamma^2 \sin^4\theta_M + 4\omega^2\right)}. \tag{18}$$

As shown in Fig. 4b, the experimentally measured θ_H dependence of V_{ISHE} is well reproduced using Eq. 18, showing the validity of this model calculation. Here, the saturation magnetization $4\pi M_s = 0.745$ T and the magnetization angle θ_M shown in Fig. 4c for the $Ni_{81}Fe_{19}$/Pt film are obtained from the magnetic-field-angle θ_H dependence of the ferromagnetic resonance field H_{FMR} using Eqs. 11 and 14.

The above calculation enables the estimation of the spin-Hall angle $\theta_{\mathrm{SHE}} = \sigma_{\mathrm{SHE}}/\sigma_N$ of the Pt layer. When the external magnetic field is applied along the film plane, the spin current injected into the Pt layer decays along the y direction due to spin relaxation as

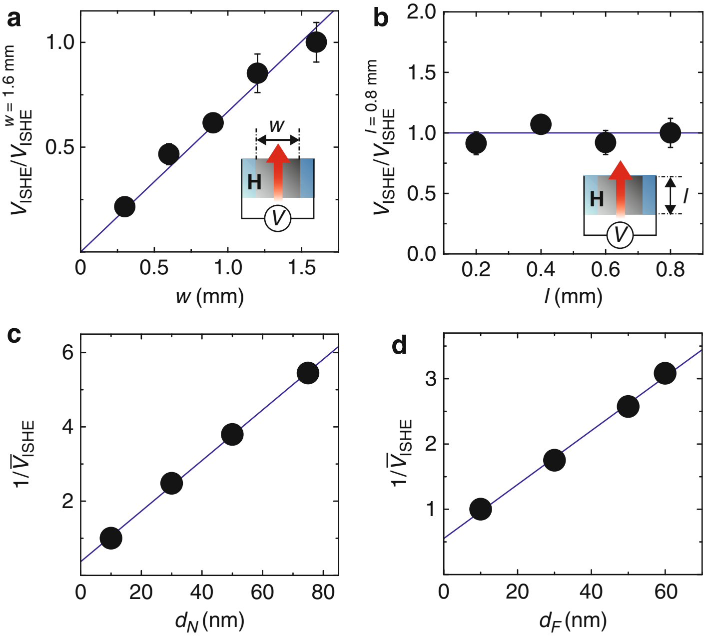

Fig. 5 (**a**) The $Ni_{81}Fe_{19}$-layer width w dependence of V_{ISHE}. w is defined as shown in the *inset*. The *solid circles* are the experimental data. The *solid line* shows the linear fit to the data. (**b**) The $Ni_{81}Fe_{19}$-layer width l dependence of V_{ISHE}. l is defined as shown in the *inset*. (**c**) The Pt layer thickness d_N dependence of V_{ISHE} when the thickness of the $Ni_{81}Fe_{19}$ layer is $d_F = 10$ nm. Here, $\overline{V}_{\mathrm{ISHE}} = V_{\mathrm{ISHE}}/V_{\mathrm{ISHE}}^{dN=dF=10\,\mathrm{nm}}$ and $V_{\mathrm{ISHE}}^{dN=dF=10\,\mathrm{nm}}$ is the magnitude of the ISHE signal when $d_N = d_F = 10$ nm. (**d**) The d_F dependence of V_{ISHE} when $d_N = 10$ nm

$$j_s(y) = \frac{\sinh[(d_N - y)/\lambda_N]}{\sinh(d_N/\lambda_N)} j_s^0, \tag{19}$$

where

$$j_s^0 = \frac{g_r^{\uparrow\downarrow}\gamma^2 h^2 \hbar \left(4\pi M_s\gamma + \sqrt{(4\pi M_s)^2\gamma^2 + 4\omega^2}\right)}{8\pi\alpha^2\left((4\pi M_s)^2\gamma^2 + 4\omega^2\right)} \tag{20}$$

is the spin current density j_s^0 at the interface ($y = 0$) obtained from Eq. 17 with $\theta_M = \pi/2$. Here, d_N and λ_N are the thickness and the spin-diffusion length of the Pt layer, respectively. The spin current $j_s(y)$ described in Eq. 19 is converted into an electromotive force V_{ISHE} using the ISHE in the Pt layer: $V_{\mathrm{ISHE}} = R_F R_N/(R_F + R_N)$ $I_c = w[\sigma_N + (d_F/d_N)\sigma_F]^{-1}\langle j_c\rangle$. Here, R_F and R_N are the electrical resistance of the $Ni_{81}Fe_{19}$ and Pt layer, respectively. $I_c \equiv l d_N \langle j_c\rangle$ is the charge current generated by the ISHE. w and l are the width and length of the $Ni_{81}Fe_{19}$ layer, respectively (see the inset to Fig. 5a, b). σ_F is the electrical conductivity of the $Ni_{81}Fe_{19}$ layer.

d_F is the thickness of the $Ni_{81}Fe_{19}$ layer. The validity of the equivalent circuit model is confirmed both from the film size and thickness dependence of the ISHE shown in Fig. 5a–d; V_{ISHE} is proportional to w and inversely linear to d_F and d_N. Using Eq. 19, we obtain the averaged charge current density defined as $\langle j_c \rangle = (1/d_N)\int_0^{d_N} j_c(y)dy$:

$$\langle j_c \rangle = \theta_{\mathrm{SHE}}\left(\frac{2e}{\hbar}\right)\frac{\lambda_N}{d_N}\tanh\left(\frac{d_N}{2\lambda_N}\right)j_s^0, \tag{21}$$

since the ISHE converts a spin current $j_s(y)$ into a charge current $j_c(y)$ as $j_c(y) = \theta_{\mathrm{SHE}}(2e/\hbar)j_s(y)$. Using Eq. 21, the electromotive force due to the ISHE induced by the spin pumping is given by

$$V_{\mathrm{ISHE}} = \frac{w\theta_{\mathrm{SHE}}\lambda_N \tanh(d_N/2\lambda_N)}{d_N\sigma_N + d_F\sigma_F}\left(\frac{2e}{\hbar}\right)j_s^0. \tag{22}$$

Using Eq. 22 with the parameters $g_r^{\uparrow\downarrow} = 2.31 \times 10^{19}\,\mathrm{m}^{-2}$, $d_N = 10$ nm, $\lambda_N = 10$ nm, [17] $\alpha = 0.0206$, $h = 0.16$ mT, $w = 1.2$ mm, $\sigma_N = 2.0 \times 10^6\ (\Omega\mathrm{m})^{-1}$, $\sigma_F = 1.5 \times 10^6\ (\Omega\mathrm{m})^{-1}$, and $V_{\mathrm{ISHE}} = 37\ \mu$V, the spin-Hall angle of the Pt layer is estimated as $\theta_{\mathrm{SHE}} = 0.04$ [7].

Magnetization-Precession Trajectory and Spin Pumping: Universality of Spin Pumping

The spin current density generated by the spin pumping is not constant when changing the out-of-plane magnetic-field angle, even for constant microwave power; the spin current density is maximized when the external magnetic field is applied oblique to the film plane. When the external magnetic field is applied oblique to the film plane, the magnetization-precession trajectory, the trajectory of the point of a magnetization vector is distorted due to a demagnetization field. It is natural to expect that the spin pumping is related to the trajectory of magnetization precession, since the spin pumping creates a spin current from magnetization precession. Let $\tilde{j}_s \equiv j_s/j_s^{\theta_H=\theta_H=0}$ be normalized spin current density, where $j_s^{\theta_H=\theta_H=0}$ is the spin current density when the magnetization precesses in a circular orbit (the external magnetic field is applied perpendicular film plane: $\theta_H = \theta_M = 0$). From Eq. 17, $\tilde{j}_s$ is obtained as

$$\tilde{j}_s = \frac{2\omega\left(4\pi M_s\gamma\sin^2\theta_M + \sqrt{(4\pi M_s)^2\gamma^2\sin^4\theta_M + 4\omega^2}\right)}{(4\pi M_s)^2\gamma^2\sin^4\theta_M + 4\omega^2}. \tag{23}$$

Equation 23 shows that $\tilde{J}_s$ strongly depends on the magnetization angle θ_M and the saturation magnetization $4\pi M_s$; $\tilde{J}_s$ is maximized when

$$\sin\theta_M = 3^{-1/4}\sqrt{\frac{2\omega}{4\pi M_s\gamma}} \tag{24}$$

is satisfied.

A magnetization-precession trajectory can be characterized in terms of the ellipticity of a magnetization-precession trajectory $A = |m_y|/|m_x|$, where $|m_x|$ and $|m_y|$ are the major and minor radiuses of the trajectory, respectively. Using Eqs. 15 and 16, the ellipticity is obtained as

$$A = \frac{2\omega}{4\pi M_s\gamma\sin^2\theta_M + \sqrt{(4\pi M_s)^2\gamma^2\sin^4\theta_M + 4\omega^2}}. \tag{25}$$

The relation between the spin current amplitude $\tilde{j}_s$ and the ellipticity, A, of a magnetization-precession trajectory is obtained by combining Eqs. 23 and 25, which is expressed as

$$\tilde{j}_s = \frac{4A}{\left(1 + A^2\right)^2}. \tag{26}$$

This simple expression indicates that the amplitude of a spin current is maximized when the precession trajectory is distorted: $A = 1/\sqrt{3}$.

A magnetization-precession trajectory is also characterized by the elliptical area of a magnetization-precession trajectory, $S = \pi|m_x||m_y|$. The normalized area of a magnetization-precession trajectory, $\tilde{S} = S/S^{\theta_H=\theta_M=0}$, is obtained using Eqs. 15 and 16 as

$$\tilde{S} = \frac{2\omega\left(4\pi M_s\gamma\sin^2\theta_M + \sqrt{(4\pi M_s)^2\gamma^2\sin^4\theta_M + 4\omega^2}\right)}{(4\pi M_s)^2\gamma^2\sin^4\theta_M + 4\omega^2}. \tag{27}$$

Here, $S^{\theta_H=\theta_M=0}$ is the area of the magnetization-precession trajectory when the magnetization precesses in a circular orbit. This expression of $\tilde{S}$ is exactly the same as that of the normalized spin current density $\tilde{j}_s$ in Eq. 23; the spin current density $\tilde{j}_s$ is determined by the elliptical area of a magnetization-precession trajectory $\tilde{S}$.

The validity of the above results can be confirmed by measuring the out-of-plane magnetic-field-angle dependence of the spin pumping using the ISHE. Figure 6b shows the magnetization-angle θ_M dependence of $\tilde{V}_{\mathrm{ISHE}} = V_{\mathrm{ISHE}}/\sin\theta_M$ for the $Ni_{81}Fe_{19}$/Pt film and a Ni/Pt film. Here, note that $\tilde{V}_{\mathrm{ISHE}}$ is proportional to the spin current density j_s generated by the spin pumping because of the relation $V_{\mathrm{ISHE}} \propto j_s \sin\theta_M$. The magnetization-angle θ_M shown in Fig. 6a is estimated from the external-magnetic-field-angle θ_H dependence of the resonance field H_{FMR} using Eqs. 11 and 14. The experimentally measured magnetization-angle θ_M dependence of $\tilde{V}_{\mathrm{ISHE}}$ is well reproduced using Eq. 23 both for $Ni_{81}Fe_{19}$/Pt film and a Ni/Pt film, showing

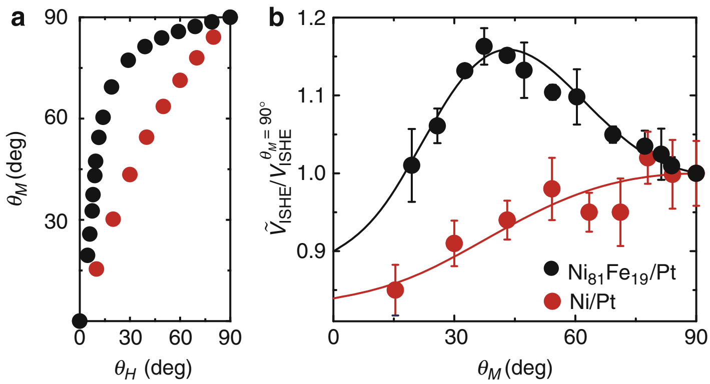

Fig. 6 (**a**) The θ_H dependence of the magnetization angle θ_M. (**b**) The magnetization-angle θ_M dependence of the spin-pumping efficiency $\tilde{V}_{\mathrm{ISHE}}/V_{\mathrm{ISHE}}^{\theta_M=90°}$ for the $Ni_{81}Fe_{19}$/Pt (*black*) and Ni/Pt films (*red*), where $\tilde{V}_{\mathrm{ISHE}} = V_{\mathrm{ISHE}}/\sin\theta_M$. $V_{\mathrm{ISHE}}^{\theta_M=90°}$ is the ISHE signal measured when $\theta_H = 90°$. The solid curve shows the theoretical curve proportional to Eq. 23

that the optimum condition for spin current generation is determined by the ellipticity of the magnetization-precession trajectory.

The relation between spin current density generated by the spin pumping and magnetization-precession trajectory can further be simplified by defining the solid angle of magnetization precession as $\Omega = S/M_s^2$. The spin current density described in Eq. 17 is expressed as

$$j_s = \frac{g_r^{\uparrow\downarrow}\omega\hbar}{4\pi}\Omega. \tag{28}$$

For metallic interfaces, the spin-pumping conductance is proportional to $n^{2/3}$, where n is the density of electrons per spin in the paramagnetic layer [18]; the spin current density in a ferromagnetic metal/Pt interface obtained by the spin pumping is determined by the solid angle Ω : $j_s \propto \Omega$. This universality has been confirmed in ferromagnetic metal/Pt interfaces using the ISHE. Figure 7 shows the relation between the spin current density j_s generated by the spin pumping and the solid angle Ω of the magnetization precession in Ni_xFe_{1-x}/Pt films, where j_s was estimated from the magnitude of the ISHE voltage. j_s is proportional to Ω as shown in Fig. 7 for all the samples, demonstrating the universality of the relation $j_s \propto \Omega$.

Spin Injection into Semiconductor by Spin Pumping

Spin injection into solids is crucial for exploring physics and technology of spin currents. However, electrical spin injection through an ohmic contact from ferromagnetic metals into high-resistivity materials, such as semiconductors and organic materials, is not easy compared with electrical spin injection into nonmagnetic

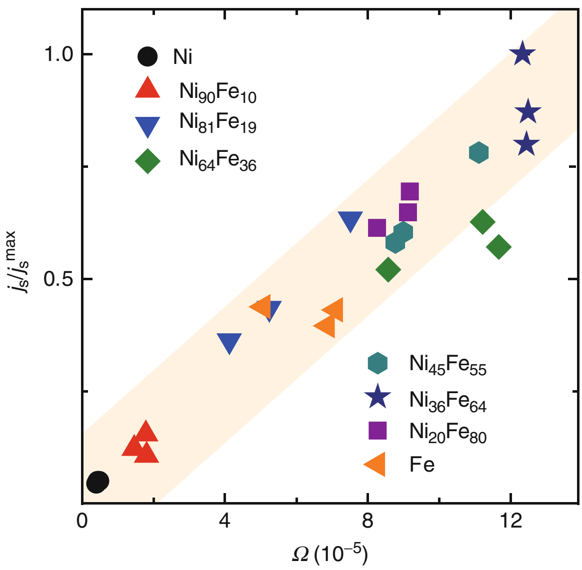

Fig. 7 Universality of the spin pumping in Ni_xFe_{1-x}/Pt films, where $x = 0$, 0.20, 0.36, 0.45, 0.64, 0.81, 0.90, and 1.0. The solid angle Ω was calculated using the parameters, including the saturation magnetization and Gilbert damping constant, obtained from FMR spectra. The spin current density j_s was estimated from the magnitude of the ISHE signal

metals. One reason is that virtually all of the applied potential drops over the high-resistivity nonmagnetic part and is wasted for spin injection. The dynamical spin-injection mechanism does not rely on an applied bias and does not suffer from the conductivity mismatch, because the smallness of the mixing conductance for a ferromagnet-semiconductor interface is compensated by the small spin current that is necessary to saturate the spin accumulation [19]. In fact, the spin pumping allows spin current injection into GaAs from $Ni_{81}Fe_{19}$ through an ohmic contact at room temperature [20].

Spin injection into GaAs using the spin pumping was demonstrated in a $Ni_{81}Fe_{19}$/Zn-doped GaAs (a $Ni_{81}Fe_{19}$/p-GaAs film) with a doping concentration of $N_A = 1.4 \times 10^{19}$ cm^{-3}. Current-voltage characteristic shown in Fig. 8a indicates the formation of an ohmic contact at the $Ni_{81}Fe_{19}$/p-GaAs interface. The ratio of the electrical conductivity for the p-GaAs layer σ_N to that for the $Ni_{81}Fe_{19}$ layer σ_F, $\sigma_N/\sigma_F = 9.7 \times 10^{-3}$ shows that the impedance-mismatch problem is critical in this system. In the $Ni_{81}Fe_{19}$/p-GaAs junction, if the dynamical exchange interaction between the magnetization in the $Ni_{81}Fe_{19}$ layer and carrier spins in the p-GaAs layer drives the spin pumping, this injected spin current induces an electromotive force through the ISHE in the GaAs layer in the FMR condition.

Figure 8b, c show microwave absorption and electromotive force signals measured for the $Ni_{81}Fe_{19}$/p-GaAs film. As shown in Fig. 8c, an electromotive force signal appears around the resonance field H_{FMR}. Here, $V(\theta)$ is defined as the asymmetric component of V with respect to $\mathbf{H}$, $V(\theta) = \left(\tilde{V}^{\theta} - \tilde{V}^{\theta+180^\circ}\right)/2$, to eliminate heating effects arising from the microwave absorption from the V spectra. $\tilde{V}^{\theta}$ and $\tilde{V}^{\theta+180^\circ}$ are the electromotive force V measured when the external magnetic field is applied at an out-of-plane angle of θ and $\theta + 180^\circ$ to the film plane,

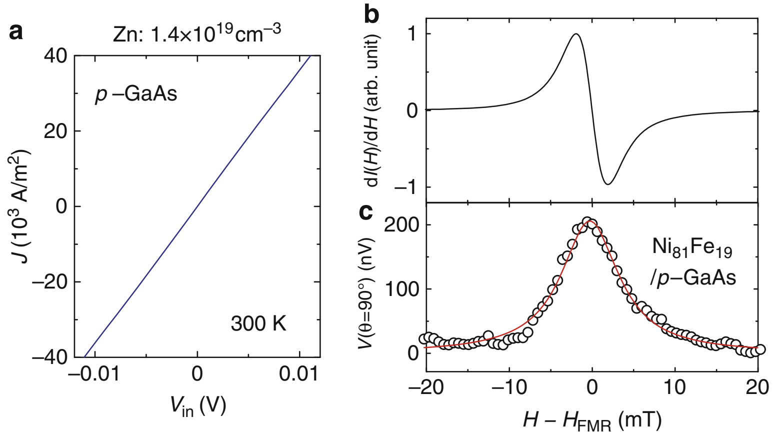

Fig. 8 (**a**) Bias voltage V_{in} dependence of current density J through the $Ni_{81}Fe_{19}$/p-GaAs junction. (**b**) Field (H) dependence of the FMR signal $dI(H)/dH$ measured for the $Ni_{81}Fe_{19}$/p-GaAs film when the external magnetic field **H** is applied along the film plane ($\theta = 90°$) (**c**) Field dependence of the electromotive force $V(\theta = 90°)$ measured for the $Ni_{81}Fe_{19}$/p-GaAs film under the 200 mW microwave excitation. Here, $V(\theta) \equiv \left(\tilde{V}^{\theta} - \tilde{V}^{\theta+180°}\right)/2$, where $\tilde{V}^{\theta}$ and $\tilde{V}^{\theta+180°}$ are the electromotive force V measured when **H** is applied at an angle of θ and θ +180° to the film plane, respectively. The *open circles* are the experimental data. The solid curve shows the fitting result using a Lorentz function

respectively. Importantly, the electromotive force signal is well reproduced using a Lorentz function, a feature expected for the spin-pumping-induced ISHE. Thus the observed electric voltage is the direct evidence of spin injection into the GaAs layer from the $Ni_{81}Fe_{19}$ layer through the ohmic interface.

Microwave power and magnetic-field-angle dependence of the electromotive force provides further evidence that the observed electric voltage is attributed to the spin injection into the GaAs layer by the spin pumping. Figure 9a shows $V(\theta = 90°)$ at different microwave excitation powers P_{MW}. The electric voltage decreases with decreasing P_{MW}, consistent with the prediction of the spin pumping. In fact, the magnitude of the electric voltage, V_{ISHE}, is proportional to P_{MW} as shown in Fig. 9b, showing that the electric voltage is attributed to the direct-current component of the spin pumping. The out-of-plane magnetic-field-angle dependence of the electromotive force shown in Fig. 10a, b provides further evidence of the dynamical spin injection into the GaAs layer.

The spin pumping driven by the dynamical spin-exchange coupling can be controlled electrically. Figure 11a shows the band structure of a $Ni_{81}Fe_{19}$ /p-GaAs interface with the bias voltage V_{in}. Here, the doping concentration of the p-GaAs layer is $N_A = 4.1 \times 10^{17}$ cm^{-3}, resulting the formation of a Schottky barrier at the interface. When $V_{in} < 0$, the depletion region and potential barrier increase, reducing spin exchange at the interface. In contrast, when $V_{in} > 0$, the depletion region and potential barrier decrease, giving rise to strong exchange interaction.

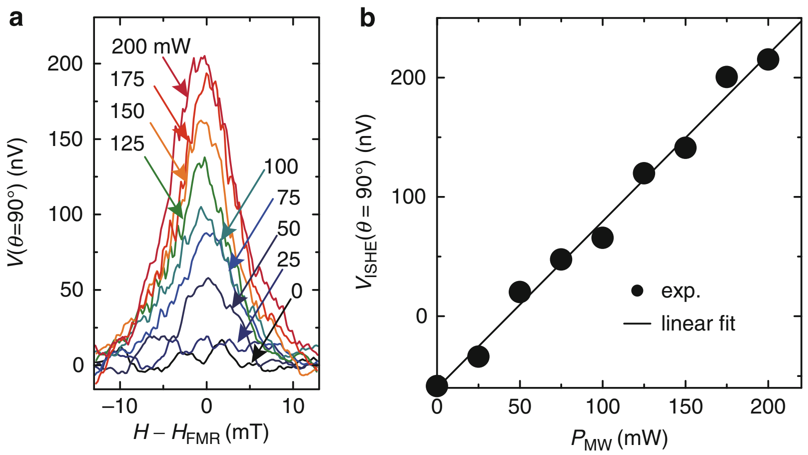

Fig. 9 (**a**) Field dependence of $V(\theta = 90°)$ measured for the $Ni_{81}Fe_{19}$/p-GaAs at different microwave excitation powers. (**b**) Microwave power P_{MW} dependence of $V_{ISHE}(\theta = 90°)$. The *solid circles* are the experimental data. The *solid lines* show the linear fit to the data

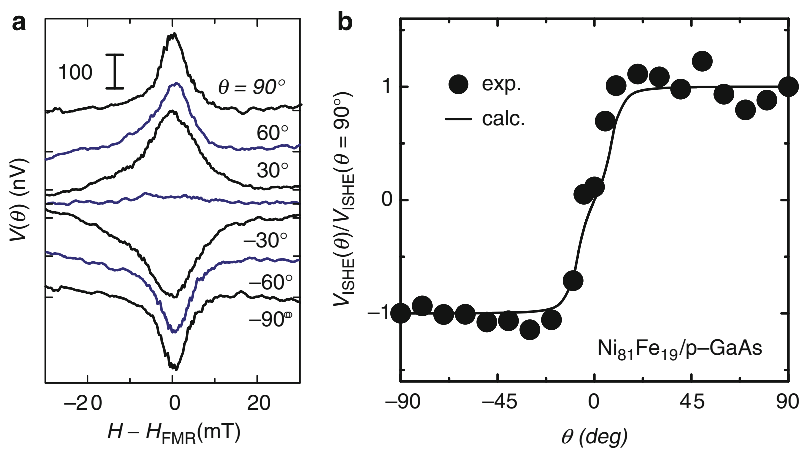

Fig. 10 (**a**) The magnetic-field-angle θ dependence of $V(\theta)$ for the $Ni_{81}Fe_{19}$/p-GaAs film. (**b**) The magnetic-field-angle θ dependence of $V_{ISHE}(\theta)/V_{ISHE}(\theta = 90°)$. The *solid circles* are the experimental data. The solid curve is the theoretical curve

The ISHE induced by the spin pumping in the Schottky $Ni_{81}Fe_{19}$/p-GaAs system was measured with applying V_{in} across the interface.

Figure 11b shows the spin-pumping conductance $g_r^{\uparrow\downarrow}$, or the spin-pumping efficiency, for the $Ni_{81}Fe_{19}$/p-GaAs junction estimated from the magnitude of the electromotive force due to the ISHE with the assumption that electric-field effects on spin diffusion are negligibly small, because the applied field is sufficiently small

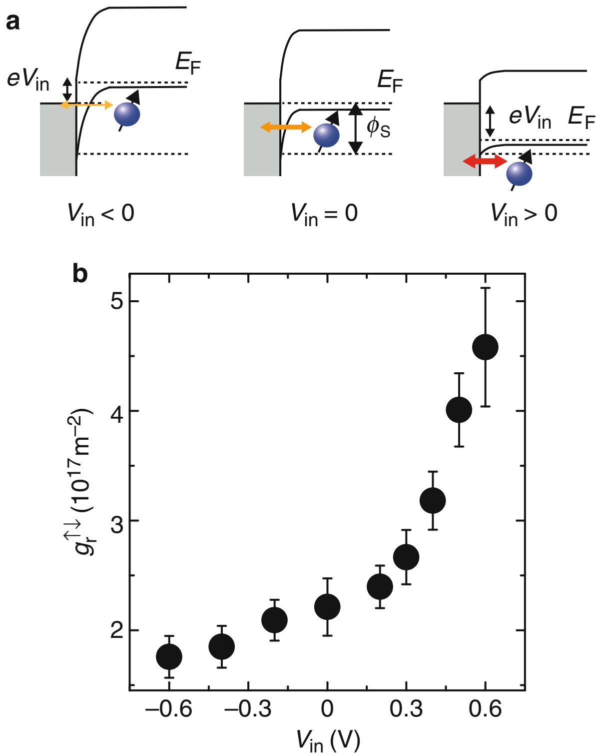

Fig. 11 (**a**) Schematic illustrations of the band structure of the $Ni_{81}Fe_{19}$/p-GaAs junction for the bias voltage $V_{in} < 0$, $V_{in} = 0$, and $V_{in} > 0$. ϕ_S is the Schottky barrier height. E_F is the Fermi level. (**b**) Bias voltage V_{in} dependence of the spin-pumping conductance $g_r^{\uparrow\downarrow}$ estimated from the measured voltage $V_{ISHE}(\theta = 90°)$ for the $Ni_{81}Fe_{19}$/p-GaAs junction at $P_{MW} = 200$ mW. $g_r^{\uparrow\downarrow}$ was estimated from the height of the electromotive force induced by the spin pumping and ISHE; the background voltage due to the ordinary Hall effect is ruled out in this estimation

in this system. The spin-pumping efficiency decreases with decreasing V_{in} when $V_{in} < 0$. When $V_{in} > 0$, in contrast, the efficiency increases with the bias voltage V_{in}. These results are consistent with the above prediction: the dynamical exchange interaction is enhanced by reducing the barrier width and height. The saturation magnetization $4\pi M_s$ is independent of V_{in}, showing that heating effects are negligibly small in this measurement because heating decreases $4\pi M_s$. Current-induced effects, such as the ordinary Hall effect, are also irrelevant; the electric voltage is independent of V_{in} when $P_{MW} = 0$ and the observed change of $V_{ISHE}(\theta = 90°)$ when $P_{MW} = 200$ mW is not linear to the bias current J, confirming that the spin-pumping efficiency is controlled electrically by applying a bias voltage.

Spin Pumping from Insulator

The above experiments demonstrate the generation of spin currents from ferromagnetic metal using the spin pumping. The origin of the spin pumping is the spin exchange at the ferromagnetic metal/paramagnetic material interfaces. This coupling was found to be finite in a ferrimagnetic insulator $Y_3Fe_5O_{12}$/paramagnetic metal Pt interface; the spin pumping appears even in an insulator/metal junction [4].

Fig. 12 (**a**) Field (H) dependence of $dI(H)/dH$ measured for the Pt/La:YIG film at $P_{MW} = 2$ mW, where I denotes the microwave absorption intensity. (**b**) Field (H) dependence of V measured for the $Y_3Fe_5O_{12}$/Pt film at $P_{MW} = 2$ mW. Here, the sign of the electromotive force is reversed by reversing the external-magnetic-field direction (see the *black* and *red curves*)

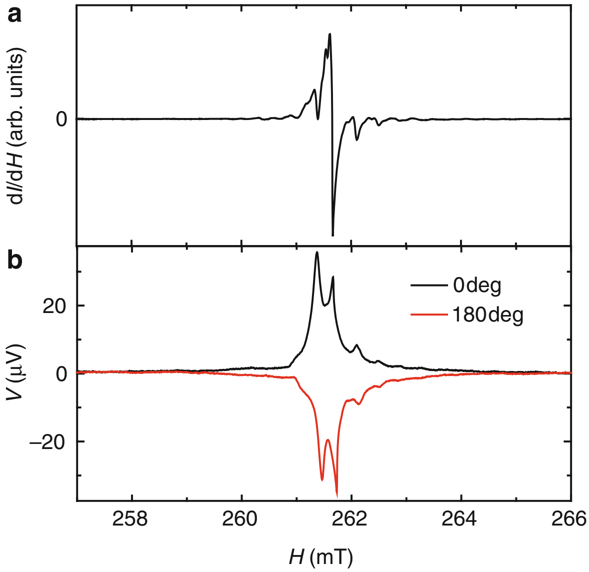

$Y_3Fe_5O_{12}$ is a ferrimagnetic insulator whose charge gap is 2.7 eV. Owing to this huge gap, $Y_3Fe_5O_{12}$ exhibits very high resistivity (~10^{12} Ωcm at room temperature, greater than that of air). A single-crystal $Y_3Fe_5O_{12}$ (111) was grown on a $Gd_3Ga_5O_{12}$ (111) single-crystal substrate by liquid phase epitaxy. The thickness of the $Y_3Fe_5O_{12}$ layer is 2.1 μm. Then, a 10-nm-thick Pt layer was sputtered on the $Y_3Fe_5O_{12}$ layer. The sample has a rectangular shape with the width 1 mm and the length 4 mm. Two electrodes were attached to the edges of the Pt layer.

Figure 12a, b are the microwave absorption dI/dH and electromotive force V signals for the $Y_3Fe_5O_{12}$/Pt film at $P_{MW} = 1$ mW, respectively, both measured with microwaves applied and with the external magnetic field perpendicular to the direction across the electrodes. In the dI/dH spectrum, many resonance signals appear. These resonance signals are attributed to the spin wave resonance in the $Y_3Fe_5O_{12}$ layer. Here, the resonance fields are much greater than the in-plane magnetization saturation field ($H_c = 20$ Oe) of this $Y_3Fe_5O_{12}$ film. Notably, at the spin wave resonance fields, electromotive force signals also appear as shown in Fig. 12b, indicating that the electromotive force is induced in the Pt layer concomitant with spin wave resonance in the $Y_3Fe_5O_{12}$ layer. As shown in Fig. 12b, the electromotive force changes its sign when the magnetic-field direction is reversed, a feature expected for the spin pumping and ISHE. Furthermore, this voltage signal was found to disappear in a $Y_3Fe_5O_{12}$/Cu system, where the Pt layer is replaced by a Cu layer, indicating the important role of spin-orbit interaction, or ISHE, in the voltage generation, since the spin-orbit interaction in Cu is very weak compared with that in Pt. The voltage signal also disappears when an insulating SiO_2 layer is inserted into the $Y_3Fe_5O_{12}$/Pt interface and when the $Y_3Fe_5O_{12}$ layer is missing. These last two results indicate that the direct contact between the $Y_3Fe_5O_{12}$ layer

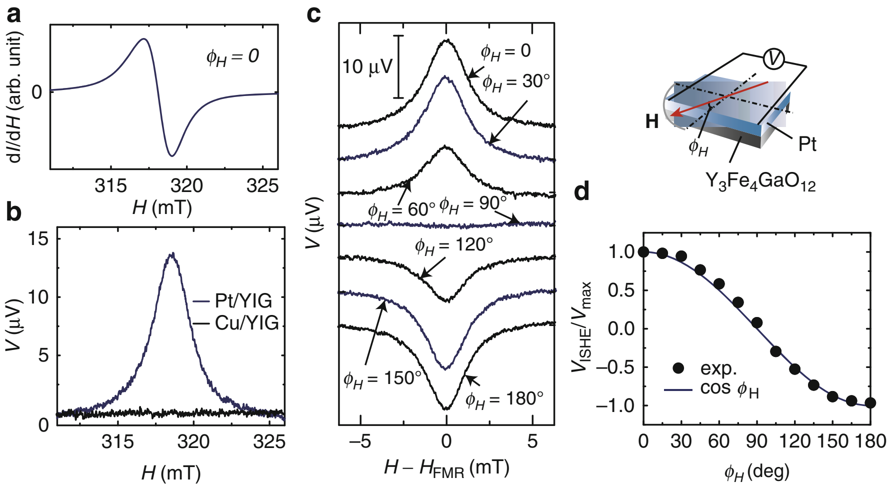

Fig. 13 (**a**) Field (H) dependence of the microwave absorption signal $dI(H)/dH$. (**b**) H dependence of the electric-potential difference V for the Pt/$Y_3Fe_4GaO_{12}$ (Pt/YIG) film (*blue curve*) and the Cu/$Y_3Fe_4GaO_{12}$ (Cu/YIG) film (*black curve*) under the 200 mW microwave excitation. (**c**) The in-plane magnetic-field-angle ϕ_H dependence of V for the Pt/$Y_3Fe_4GaO_{12}$ film. (**d**) The in-plane magnetic-field-angle ϕ_H dependence of the ISHE signal measured for the Pt/$Y_3Fe_4GaO_{12}$ film. V_{ISHE}/V_{max} is the normalized spectral intensity. The *filled circles* are the experimental data. The solid curve shows cos ϕ_H

and the Pt layer is necessary for the observed voltage generation; electromagnetic artifacts are irrelevant.

The spin pumping in the $Y_3Fe_5O_{12}$/Pt film can be attributed to the small but finite spin-exchange interaction between a conduction electron in the Pt layer and a localized moment in the $Y_3Fe_5O_{12}$ layer or to the spin-pumping conductance at the interface. The spin pumping at an insulator/metal interface exists not only in a single-crystal insulator/Pt interface but also in a polycrystal insulator/Pt interface.

A polycrystal 100-nm-thick $Y_3Fe_4GaO_{12}$ film was grown on a $Gd_3Ga_5O_{12}$ (111) single-crystal substrate by metal organic decomposition. Then, a 10-nm-thick Pt layer was sputtered on the $Y_3Fe_4GaO_{12}$ layer. Immediately before the sputtering, the surface of the $Y_3Fe_4GaO_{12}$ film was cleaned by Ar-ion bombardment in a vacuum.

Figure 13a, b shows the microwave absorption signal $dI(H)/dH$ and the electric-potential difference V measured for the $Y_3Fe_4GaO_{12}$/Pt film when $\phi_H = 0$, where $\phi_H = 0$ is the in-plane magnetic-field angle defined as in the inset to Fig. 13. In the V spectrum, an electromotive force signal appears around the resonance field. This electromotive force is disappeared in a Cu/$Y_3Fe_4GaO_{12}$ film, providing the evidence that the electromotive force is attributed to the ISHE induced by the spin pumping. In fact, the electromotive force varies systematically by changing the in-plane magnetic-field angle as shown in Fig. 13c, which is consistent with the prediction of the spin-pumping-induced ISHE; V_{ISHE} disappears at $\phi_H = 90°$ and changes its sign at $90° < \phi_H < 180°$. Notably, as shown in Fig. 13d, this variation is well reproduced using $\cos \phi_H$, being consistent with Eq. 6; since the spin polarization σ of the dc component of a spin current generated by the spin pumping is directed along the magnetization-precession axis, or the external-magnetic-field direction, Eq. 6 predicts $V_{\mathrm{ISHE}} \propto |\mathbf{j}_s \times \sigma|_x \propto \cos \phi_H$. Here, $|\mathbf{j}_s \times \sigma|_x$ denotes the x component of $\mathbf{j}_s \times \sigma$.

Nonlinear Spin Pumping

The very small magnetic damping of $Y_3Fe_5O_{12}$ offers a way for exploring nonlinear effects of the spin pumping. Figure 14a shows electromotive force V spectra at various microwave excitation power P_{MW} for a Pt/La-substituted $Y_3Fe_5O_{12}$ (Pt/La:YIG) bilayer film. Here, the single-crystal La:YIG (111) film with a thickness of 2 μm was grown on a $Gd_3Ga_5O_{12}$ (111) substrate by liquid phase epitaxy, where La was substituted to match the lattice constant between the film and the substrate. Figure 14a shows that electromotive force appears around the ferromagnetic

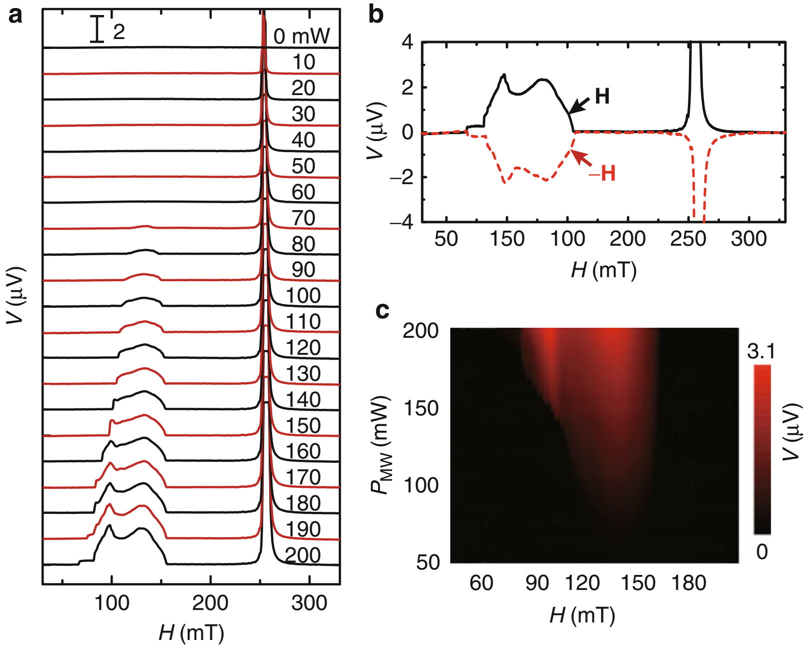

Fig. 14 (**a**) Field (H) dependence of the electromotive force V measured for the Pt/La:YIG film at various microwave excitation power P_{MW}. (**b**) Field (H) dependence of V measured for the Pt/La:YIG film at $P_{\mathrm{MW}} = 200$ mW. Here, the sign of the electromotive force is reversed by reversing the external-magnetic-field direction (see the *black* and *red curves*). (**c**) A contour plot of the electromotive force V as a function of the external magnetic field H and the microwave power P_{MW}

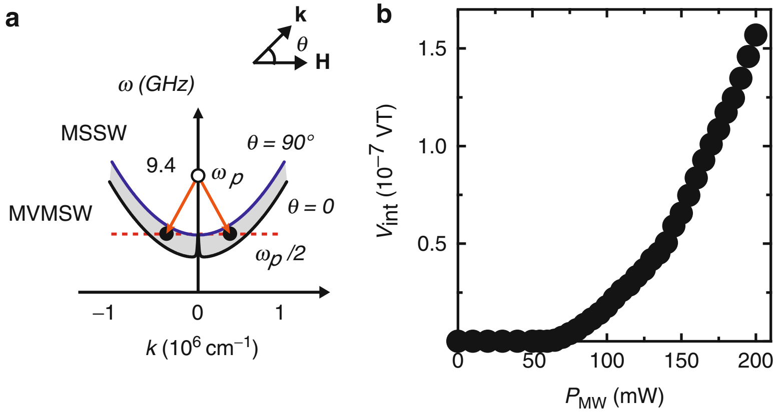

Fig. 15 (**a**) The spin wave dispersion for the Pt/La:YIG film when the parametric excitation condition. θ represents the angle between **H** and **k**. (**b**) Microwave power P_{MW} dependence of the field-integrated intensities, V_{int}, for the V spectra

resonance field $H_{\mathrm{FMR}} \approx 250$ mT, which is induced by the spin pumping from the La:YIG layer to the Pt layer (see also Fig. 14b).

The most notable feature of the V spectra is found when exploring the high-power response of these signals around $H = 120$ mT. Figure 14a shows that an electromotive force signal appears also far below H_{FMR} when $P_{\mathrm{MW}} \geq 70$ mW. This electromotive force changes its sign by reversing the magnetic-field direction (see Fig. 14b), indicating that the electromotive force is attributed to the ISHE induced by spin current injection into the Pt layer.

The electromotive force observed here is induced by the spin pumping driven by parametrically excited spin waves. Spin waves with the wavevector $\mathbf{k} \neq \mathbf{0}$ can be excited through a magnon-magnon interaction; when the microwave magnetic field with frequency $\omega_p = 2\pi f$ is applied perpendicular to the static magnetic field $\mathbf{H}$, as shown in Fig. 15a, a pair of modes $\mathbf{k}$ and $-\mathbf{k}$ which satisfy the resonance condition $\omega_{\mathbf{k}} = \omega_{-\mathbf{k}} = \omega_p/2$ are excited parametrically via a uniform virtual state ($\mathbf{k} = \mathbf{0}$) using the three-magnon interaction, which gives subsidiary absorption shown in Fig. 14a [21–24]. The number of generated magnons grows exponentially, when the pumping field exceeds a certain threshold, i.e., when a pair of modes are fed sufficient energy to overcome the dissipation. In the P dependence of the field-integrated intensities for the V spectra shown in Fig. 15b, V_{int}, a clear threshold is observed around $P_{\mathrm{MW}} =$ 70 mW, demonstrating nonlinear generation of spin currents. The contour plot of the electromotive force V as a function of the external magnetic field H and the microwave power P_{MW} in Fig. 14c also supports the above scenario; the contour plot of shows a butterfly structure as expected for the parametric excitation of spin waves [22], indicating that the three-magnon interaction is responsible for the nonlinear spin pumping. Since nonlinear phenomena in condensed matter have played crucial roles in the development of active elements in electronics, these results will be essential for developing nonlinear spintronic devices, such as a spin current amplifier.

Summary

The spin pumping offers a route for generating spin currents in nonmagnetic materials. Because the spin-pumping method requires only magnetization precession in a ferromagnetic/nonmagnetic junction for the spin injection, it can be combined with a wide range of ferromagnetic resonance excitation elements, for example, spin torque oscillators, enabling integration of this method into spintronic devices. Thus, this new spin-injection approach will pave the way toward the creation of room-temperature spintronic devices in a large selection of materials, promising important advances in the field of spintronics.

References

1. Slonczewski JC (1996) Current-driven excitation of magnetic multilayers. J Magn Magn Mater 159:L1
2. Tserkovnyak Y, Brataas A, Bauer GEW (2002) Enhanced Gilbert damping in thin ferromagnetic films. Phys Rev Lett 88:117601
3. Mizukami S, Ando Y, Miyazaki T (2002) Effect of spin diffusion on Gilbert damping for a very thin permalloy layer in Cu/permalloy/Cu/Pt films. Phys Rev B 66:104413
4. Kajiwara Y, Harii K, Takahashi S, Ohe J, Uchida K, Mizuguchi M, Umezawa H, Kawai H, Ando K, Takanashi K, Maekawa S, Saitoh E (2010) Transmission of electrical signals by spin-wave interconversion in a magnetic insulator. Nature 464:262
5. Saitoh E, Ueda M, Miyajima H, Tatara G (2006) Conversion of spin current into charge current at room temperature: Inverse spin-Hall effect. Appl Phys Lett 88:182509
6. Ando K, Kajiwara Y, Takahashi S, Maekawa S, Takemoto K, Takatsu M, Saitoh E (2008) Angular dependence of inverse spin–Hall effect induced by spin pumping investigated in a $Ni_{81}Fe_{19}$/Pt thin film. Phys Rev B 78:014413
7. Ando K, Takahashi S, Ieda J, Kajiwara Y, Nakayama H, Yoshino T, Harii K, Fujikawa Y, Matsuo M, Maekawa S, Saitoh E (2011) Inverse spin-Hall effect induced by spin pumping in metallic system. J Appl Phys 109(10):103913
8. Morrish AH (1980) The physical principles of magnetism. Robert E. Krieger, New York
9. Tserkovnyak Y, Brataas A, Bauer GEW, Halperin BI (2005) Nonlocal magnetization dynamics in ferromagnetic heterostructures. Rev Mod Phys 77:1375
10. Mosendz O, Pearson JE, Fradin FY, Bauer GEW, Bader SD, Hoffmann A (2010) Quantifying Spin Hall Angles from Spin Pumping: Experiments and Theory. Phys Rev Lett 104(4):046601
11. Ando K, Takahashi S, Harii K, Sasage K, Ieda J, Maekawa S, Saitoh E (2008) Electric manipulation of spin relaxation using the spin Hall effect. Phys Rev Lett 101:036601
12. Tannenwald PE, Seavey MH Jr (1959) Microwave resonance in thin ferromagnetic films. J Phys Radium 20:323
13. Juretschke HJ (1960) Electromagnetic theory of dc effects in ferromagnetic resonance. J Appl Phys 31:1401
14. Chazalviel JN, Solomon I (1972) Experimental evidence of the anomalous Hall effect in a nonmagnetic semiconductor. Phys Rev Lett 29:1676
15. Inoue HY, Harii K, Ando K, Sasage K, Saitoh E (2007) Detection of pure inverse spin-Hall effect induced by spin pumping at various excitation. J Appl Phys 102:083915
16. Silsbee RH, Janossy A, Monod P (1979) Coupling between ferromagnetic and conduction-spin-resonance modes at a ferromagnetic—normal-metal interface. Phys Rev B 19:4382
17. Vila L, Kimura T, Otani Y (2007) Evolution of the Spin Hall Effect in Pt Nanowires: Size and Temperature Effects. Phys Rev Lett 99(22):226604

18. Heinrich B, Tserkovnyak Y, Woltersdorf G, Brataas A, Urban R, Bauer GEW (2003) Dynamic exchange coupling in magnetic bilayers. Phys Rev Lett 90:187601
19. Brataas A, Tserkovnyak Y, Bauer GEW, Halperin BI (2002) Spin battery operated by ferromagnetic resonance. Phys Rev B 66:060404(R)
20. Ando K, Takahashi S, Ieda J, Kurebayashi H, Trypiniotis T, Barnes CHW, Maekawa S, Saitoh E (2011) Electrically tunable spin injector free from the impedance mismatch problem. Nat Mater 10:655
21. L'vov VS (1994) Wave turbulence under parametric excitation. Springer, Berlin
22. Suhl H (1957) The theory of ferromagnetic resonance at high signal powers. J Phys Chem Solids 1:209
23. Rezende S, de Aguiar F (1990) Spin-wave instabilities, auto-oscillations, and chaos in yttrium-iron-garnet. Proc IEEE 78(6):893
24. Kabos P, Wiese G, Patton CE (1994) Measurement of spin wave instability magnon distributions for subsidiary absorption in yttrium iron garnet films by Brillouin light scattering. Phys Rev Lett 72(13):2093